Journal of Natural Resources and Environmental Management
http://dx.doi.org/10.29244/jpsl.16.3.284

RESEARCH ARTICLE

OPEN ACCESS

Check for updates

Evaluating Accuracy and Temporal Consistency of Machine Learning Models for Land Use/Land Cover Mapping in the Cimanuk Watershed

Salis Deris Artikanur[a], Widiatmaka Widiatmaka[b], Wiwin Ambarwulan[a], Irmadi Nahib[ac], Darmawan Listya Cahya[a], Afifuddin[d], Yudi Setiawan[ef]

[a] Research Center for Limnology and Water Resources, National Research and Innovation Agency, Bogor, 16911, Indonesia
[b] Department of Soil Science and Land Resources, Faculty of Agriculture, IPB University, IPB Dramaga Campus, Bogor, 16680, Indonesia
[c] Study Program of Natural Resources and Environmental Management Science (NREMS), Graduate School, IPB University, Bogor, 16143, Indonesia
[d] Research Center for Geoinformatics, National Research and Innovation Agency, Bogor, 16911, Indonesia
[e] Department of Forest Resources Conservation and Ecotourism, Faculty of Forestry and Environment, IPB University, IPB Dramaga Campus, Bogor, 16680, Indonesia
[f] Center for Environmental Research, International Research Institute for Environment and Climate Change, IPB University, IPB Dramaga Campus, Bogor, 16680, Indonesia

Article History
Received 14 January 2026
Revised 9 April 2026
Accepted 10 April 2026

Keywords
accuracy improvement, classification correction, google earth engine, irrational transition detection, watershed monitoring

ABSTRACT

One of the critical watersheds in Indonesia is the Cimanuk watershed, which is recognized as a national priority watershed. Remote sensing plays a vital role in monitoring land use/land cover (LULC) in the Cimanuk watershed. Overall accuracy (OA) and Kappa coefficient (KC) are commonly used as primary measures of classification accuracy. In addition to these parameters, it is essential to examine the consistency of LULC classification over time. This study aimed to compare the accuracy and temporal consistency of three Machine Learning Models: random forest (RF), support vector machine (SVM), and classification and regression tree (CART) for LULC classification in the Cimanuk watershed using Sentinel-2 Multispectral Instrument (MSI) images for 2020 and 2025, processed in Google Earth Engine (GEE). The results indicate that RF has the highest accuracy, with 87.9% (OA) and 83.7% (KC) in 2025, and 83.6% (OA) and 77.9% (KC) in 2020. The lower classification accuracy in 2020 compared to 2025 is likely due to the 2025 image having clearer visual characteristics and better spectral separability among LULC classes. When examining inconsistent transitions between 2020 and 2025, CART accounted for 11.97% of these transitions, higher than RF and SVM. After applying temporal consistency correction to the 2020 LULC classification result, RF remains the best-performing classifier, achieving 90% (OA) and 86.5% (KC), followed by CART and SVM. These findings provide valuable insights into incorporating accuracy and temporal consistency assessments into time-series LULC analysis, serving as a reference for future LULC studies in watershed management and other geographic contexts.

Introduction

Human needs for food, water, energy, housing, infrastructure, environment, and socio-cultural aspects are increasing as the population grows [1,2]. This phenomenon drives more intensive land utilization. Monitoring land use/land cover (LULC) is essential using a functional analysis unit in the form of a watershed because a watershed reflects the holistic relationship between biophysical and social aspects. A total of 108 watersheds in Indonesia have been designated as priority watersheds due to their critical condition resulting from LULC changes, including those on Java Island [3]. Several studies have conducted LULC monitoring in Indonesian watersheds, including the Cisadane [4], Citarum [5], and Brantas [6] watersheds.

Corresponding Author: Widiatmaka Widiatmaka widiatmaka@apps.ipb.ac.id Department of Soil Science and Land Resources, Faculty of Agriculture, IPB University, IPB Dramaga Campus, Bogor, Indonesia.

One of the critical watersheds on Java Island is the Cimanuk watershed, which is considered a national priority watershed [7]. Unsustainable land use in the Cimanuk watershed has led to a decline in watershed functions, resulting in 31% of critical land areas [8]. Monitoring LULC in the Cimanuk watershed is essential for observing changes over time and promoting sustainable land-use practices. Remote sensing plays a vital role in monitoring LULC in watersheds. Many studies have conducted digital analyses of LULC changes in watersheds using the Google Earth Engine (GEE) platform [9–11]. Digital analysis using GEE is chosen because it is objective, relatively quick, and easy to replicate [12,13]. Analyzing LULC over large areas with high-resolution imagery requires substantial data, so selecting GEE can facilitate LULC classification compared to traditional analysis techniques [14].

The GEE platform supports various classifiers for LULC analysis, including random forest (RF), support vector machine (SVM), maximum likelihood (ML), classification and regression tree (CART), and minimum distance (MD) [15]. Among these, RF, SVM, and CART are widely utilized due to their effectiveness in handling multispectral remote sensing data. RF is an ensemble learning method that combines multiple decision trees via majority voting, providing high accuracy and robustness against overfitting. However, while offering higher performance, this approach demands more extensive computational resources and may limit the model interpretability [16]. SVM is a supervised algorithm that constructs optimal hyperplanes to separate classes in a high-dimensional feature space. While effective at handling limited training samples and complex class boundaries, the model's performance remains highly contingent upon the precise selection of parameter and kernel [17]. Meanwhile, CART is a tree-based method that partitions data using decision rules. It is computationally efficient and easy to interpret, though it may be prone to overfitting and sometimes yields lower accuracy than ensemble methods, such as RF [17].

The availability of multiple classifiers makes it essential to evaluate each classifier's performance to achieve accurate classifications. Previous studies have compared two or more classifiers in GEE. Prodromou et al. [18] compared classification results using three classifiers (RF, SVM, and CART). Meanwhile, Xie and Niculescu [19] compared classification results of SVM, RF, and convolutional neural network (CNN). The main parameters used to compare classifier performance are overall accuracy (OA) and Kappa coefficient (KC). These metrics reflect how well the classification results match actual land cover sample points.

However, OA and KC do not fully capture classification accuracy, especially with respect to consistency and temporal rationality. For example, a classification in year one might show built-up land, but in year two, it shows paddy fields, indicating an inconsistency or irrational change. Based on previous studies comparing LULC classification results across multiple classifiers [20,21], no analysis has examined the consistency of classification results across classifiers. Therefore, this study aims to compare the accuracy and temporal consistency of RF, SVM, and CART classifiers for LULC analysis in the Cimanuk watershed. The novelty of this research lies in obtaining spatial LULC analysis results for the Cimanuk watershed that consider the consistency of LULC change transitions across RF, SVM, and CART classifiers.

The OA and KP are commonly used metrics for evaluating the performance of LULC classification, as they measure the agreement between classified maps and reference data for a specific time period. However, these metrics do not evaluate whether the classified land-cover classes remain logically consistent across multiple time periods. In this study, temporal consistency refers to the logical continuity of LULC classes across consecutive years, where land transitions follow plausible land-use dynamics (e.g., forests converting to agriculture rather than reverting abruptly to unrelated classes). Previous studies are currently limited to the long-term temporal consistency of LULC data [22,23]. Most studies evaluate classification performance only using OA, the KC, and class-based accuracies, without assessing the consistency of changes over time in LULC maps [10,16,20]. Consequently, maps with high OA and Kappa values may still produce unrealistic LULC transitions over time. Such temporal irregularities can undermine the reliability of LULC change analysis and spatial planning.

To address this gap, this study aims to compare the accuracy and temporal consistency of three widely used classifiers: RF, SVM, as well as CART for LULC classification located in the Cimanuk watershed. By evaluating both classification accuracy and temporal consistency, this study seeks to deliver robust LULC datasets essential for informed land-use monitoring and effective watershed management. The novelty of this study lies in integrating conventional classification accuracy assessment (OA and KC) with a temporal consistency evaluation of LULC transitions derived from multi-temporal classification results. While previous studies typically compare classifiers based on accuracy metrics, such as OA and Kappa, this study introduces an

additional evaluation of the logical consistency of land-cover transitions between years. Temporal consistency was assessed by identifying irrational or unlikely transitions between consecutive years and applying a masking-based correction. This approach enables the correction of inconsistent classifications and provides a more robust comparison of RF, SVM, and CART classifiers for multi-temporal LULC analysis.

Materials and Methods

Study Area

The research was conducted in the Cimanuk watershed. The Cimanuk watershed is located in West Java Province, Indonesia. This watershed covers Garut Regency (upstream), Majalengka and Sumedang (middle-stream), and Indramayu (downstream). The Cimanuk watershed covers an area of 363,568.47 hectares and is situated at 06°13.7'–07°25.7' South Latitude and 107°42.5'–108°24.5' East Longitude [24]. The terrain in the Cimanuk watershed is predominantly less than 30% slope (about 64%), with very steep slopes found on two mountain peaks within the watershed, namely Mount Papandayan and Mount Cikuray [8]. The map of the research location in the Cimanuk watershed is presented in Figure 1.

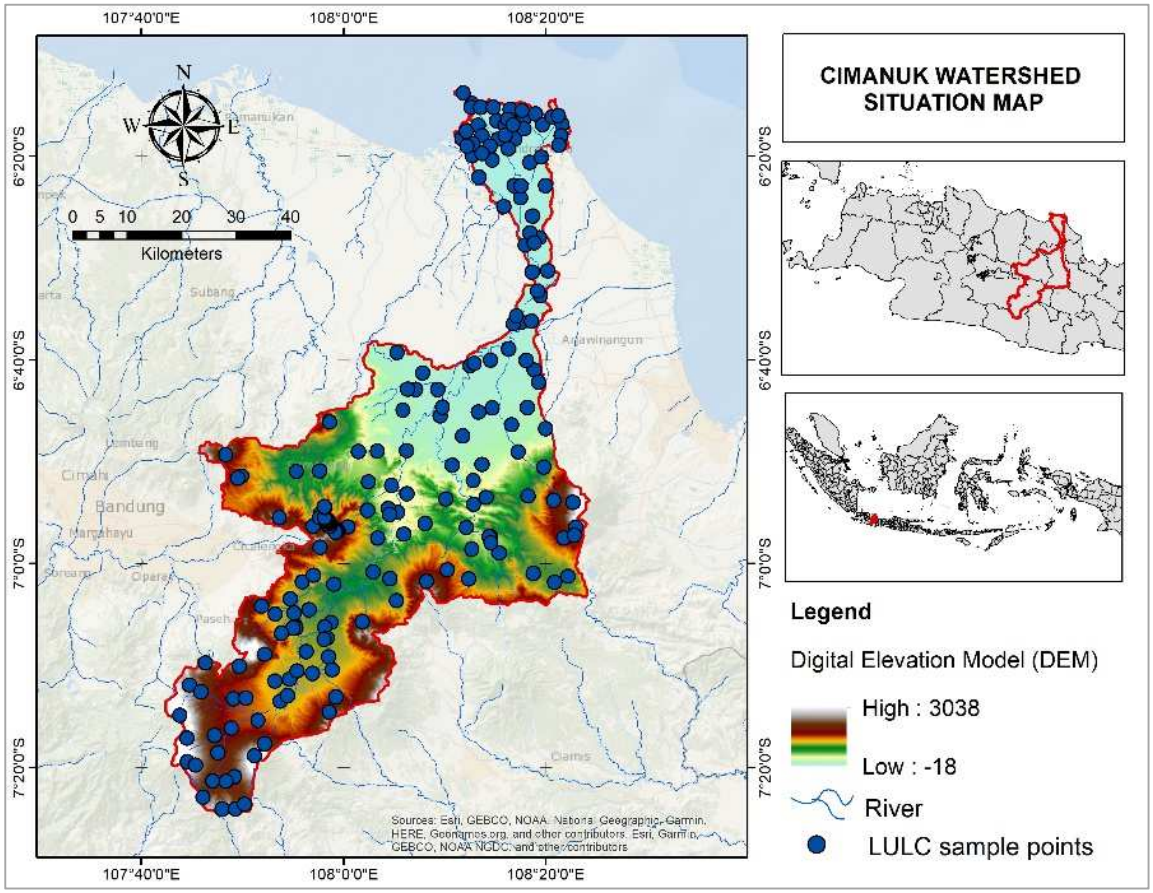

Figure 1. Map of the study area. The map shows that the highest elevation in the Cimanuk Watershed reaches 3,038 meters above sea level. Areas with high elevation are predominantly located in the southern (upstream) region, while lower elevations are found in the northern (downstream) part. The points distributed across the map represent sample locations for LULC classification, totaling 210 points, which are categorized into seven classes: built-up land (BU), dryland agriculture (DA), paddy fields (PF), plantations (PL), forests (FO), ponds (PO), and water bodies (WB).

Datasets and Sources

The data used for analyzing LULC include Sentinel-2 Multispectral Instrument (MSI) satellite images from 2020 and 2025 with a resolution of 10 meters sourced from the European Union/European Space Agency/Copernicus. LULC sample points from high-resolution satellite images obtained from Google Earth Pro. The Indonesian Topographic Map was sourced from the *Badan Informasi Geospasial* (BIG). Datasets, specifications, and sources used in this study are presented in Table 1.

Table 1. Datasets, specifications, and sources used in this study. The table summarizes the datasets employed for LULC classification in the Cimanuk Watershed, including Sentinel-2 MSI Level-2A surface reflectance data, LULC sample points derived from high-resolution Google Earth Pro imagery, and the *Rupa Bumi Indonesia* (RBI) map. It provides key specifications such as spatial resolution, acquisition periods, cloud cover threshold, and map scale, along with their respective data sources and access links.

Dataset	Specification	Source
Sentinel-2 MSI Level 2A Surface Reflectance Harmonized	Resolution: 10 meters Acquisition period of 2020: 01-01-2020 to 31-12-2020 Acquisition period of 2025: 01-01-2025 to 31-12-2025 Cloud cover: < 20%	European Space Agency (ESA) [25]
LULC sample points obtained from Google Earth Pro (high-resolution satellite imagery)	Reference years: 2020 and 2025 Used for training and validation of LULC classification Visual interpretation of LULC classes	Google Earth Pro (imagery provided by Maxar Technologies and Airbus Defence and Space) [26]
Rupa Bumi Indonesia (RBI) map	Scale 1:25,000 Area of interest: Garut, Indramayu, Majalengka, and Sumedang Regency	*Badan Informasi Spasial* (BIG) [27]

Methods

Image Pre-processing

LULC classification was conducted in 2020 and 2025 using Sentinel-2 satellite imagery at 10 meters resolution in GEE. Before performing the LULC classification, the images were filtered by Cimanuk watershed location, analysis year, and cloud cover below 20%. Additionally, cloud and cirrus masking were applied to the remaining clouds using the QA60 band of Sentinel-2 imagery. Next, sample points were input into GEE. The sample points from high-resolution Google Earth Pro images numbered 30 for each land cover/use class (a total of 210 points). A total of 30 sample points were selected for each LULC class because, based on Joyce [28], approximately 30 to 50 training sample sites are recommended for each LULC class to adequately represent the range of field conditions and spectral variability within each class. Training samples were identified using the historical imagery feature to select images that align as closely as possible with the 2020 and 2025. LULC classes were then determined through visual interpretation of color, texture, pattern, and contextual characteristics. Only locations with clearly identifiable and temporally consistent land cover were used as training and testing samples.

The LULC classes analyzed included: BU, DA, PF, PL, FO, PO, and WB. For each sample point, a polygon was digitized around it to obtain training and test pixels. The total number of pixels was 116,261, with 70% (81,155) for training and 30% (35,106) for testing. The classification bands used were 2 (blue), 3 (green), 4 (red), and 8 (near-infrared). Additionally, the Normalized Difference Vegetation Index (NDVI) and Normalized Difference Water Index (NDWI) parameters were used in the classification to achieve more accurate results. NDVI and NDWI were included as additional predictor variables because they enhance the separability of vegetation and water-related land-cover classes, thereby reducing spectral confusion and improving classification accuracy. NDVI is considered effective for distinguishing vegetated from non-vegetated areas, whereas NDWI improves the identification of water bodies and moist surfaces. Recent studies have indicated that integrating NDVI and NDWI into LULC classification significantly improves classification performance [29,30].

Land Use/Land Cover Classification

LULC classification was conducted using supervised methods with RF, SVM, and CART classifiers in GEE for the 2020 and 2025 images. The LULC for 2025 was analyzed first, given the better cloud cover in the images compared to 2020. LULC was classified into seven classes based on the sample points: BU, DA, PF, PL, FO, PO, and WB. Details regarding the RF, SVM, and CART classifiers used in this study are explained as follows:

Random forest (RF)

RF is a decision tree-based classifier developed by Breiman [31]. RF constructs random decision trees (forests), then performs majority voting to obtain a more stable and accurate classification result. The RF classifier was implemented in GEE using the smileRandomForest algorithm. The number of trees (ntree) was

set to 100, which aimed to ensure stable classification performance. Other parameters, including the number of variables per split (mtry), the maximum tree depth, and the bagging fraction, were set to their default values in GEE. In this implementation, the number of variables per split was automatically set to the square root of the total number of predictor variables, and trees were grown without a predefined maximum depth, using bootstrap aggregation (bagging) to generate robust classification results. The RF formula is presented in Equation 1 as follows:

$$\{h(x, \theta_k), k = 1, \dots\} \quad (1)$$

Where the function h represents a single decision tree. Meanwhile, k is the index of the decision tree, with values ranging from 1 to K. θ_k is a randomly distributed and independent vector, each tree contributes to the class with the highest count for input x.

Support vector machine (SVM)

SVM was developed by Cortes and Vapnik [32]. SVMs perform classification by learning from previously labeled data and predicting new data points. The main goal of using SVM is to find the best decision boundary, or the maximum-margin separating hyperplane, that separates different data categories [33]. SVM uses several kernel functions, specific formulas that help it separate classes of data that are difficult to distinguish. The kernel functions used by SVM include linear, radial basis function (RBF), polynomial, and sigmoid. This research uses the RBF kernel because, based on previous studies, it is more effective compared to other kernel functions [34]. The RBF kernel formula [35] is presented in Equation 2 as follows:

$$k(x_i, x_j) = exp(-\frac{\|x_i - x_j\|^2}{2\sigma^2}) = exp(-\gamma \|x_i - x_j\|^2) \quad (2)$$

Where $k(x_i, x_j)$ is the kernel function, x_i is the i-th data point, x_j is the j-th data point, and σ is the kernel width. Gamma (γ) is the kernel scale parameter derived from the kernel width (σ), with the relationship defined as $\gamma = 1/2\sigma^2$. When σ approaches zero, the SVM tends to overfit. Meanwhile, if σ is too large, it can cause underfitting. If γ is large, the model becomes more sensitive and the patterns more complex. If γ is small, the model is less sensitive. Therefore, the appropriate kernel width must be chosen. In this study, the SVM classifier was implemented in GEE using the LIBSVM library (*ee.Classifier.libsvm*). This was trained on a training dataset derived from the digitized sample polygons and Sentinel-2 spectral bands as input features. The RBF kernel was employed due to its efficacy in handling the nonlinear relationships in multispectral remote sensing data. Tuning was not performed in this study because it used the same reference values as the previous study by Prodromou et al. [18], which set gamma = 1 and cost (C) = 100 to control the kernel sensitivity and the penalty for misclassification, respectively. These selected parameters were used to present good classification performance.

Classification and regression tree (CART)

CART was developed by Breiman in 1984 [31], based on regression analysis and simple decision-making. A decision tree in CART is built by splitting the training data at a threshold until leaf nodes are reached that cannot be split further. Leaf nodes are used to make predictions [20]. The CART classifier uses Gini impurity, a measure of a node's impurity in a decision tree. Gini impurity is used to build the decision tree and determine the optimal decision splits. The Gini impurity formula used by CART is presented in Equation 3 [36]. Based on Equation 3, Gini (p) is the Gini impurity, pi represents the proportion of data belonging to class I, and N is the number of classes. The higher the Gini value, the less pure or the more difficult the separation between classes.

$$Gini(p) = 1 - \sum_{i=1}^{N} (pi^2) \quad (3)$$

In this study, the CART classifier was implemented in GEE using the *ee.Classifier.smileCart()* function. This was trained using LULC training samples and the selected spectral bands from the satellite imagery as input variables. The algorithm automatically generates decision rules by partitioning the feature space based on impurity reduction, commonly measured using the Gini impurity (Equation 3) [37]. After training, the resulting decision tree model was applied to classify the imagery.

Accuracy Assessment

The accuracy of LULC classification was assessed using OA and KC. OA and KC were calculated twice, before and after the consistency correction (Figure 2). The accuracy assessment was conducted in two stages: initially, following the LULC classification, and subsequently, after the masking-based temporal consistency assessment. The second assessment was conducted after the LULC correction using masking to obtain a

temporally consistent classification. The two-stage accuracy assessment was performed to quantify the effect of temporal consistency correction on OA and Kappa values. The formulas for OA and KC [38] are presented in Equations 4 and 5 as follows:

$$Overall\ Accuracy = \frac{x}{y} \times 100\% \quad (4)$$

Where x represents the LULC class results from the classification that match the field check results, and y represents the total LULC points that have been validated.

$$Kappa\ Coefficient = \frac{y\sum_{i=1}^{N} x_{ii} - \sum_{i=1}^{N}(x_{i+}x_{+i})}{y^2 - \sum_{i=1}^{N}(x_{i+}x_{+i})} \quad (5)$$

Where, x_{ii} is the LULC type-i from the simulation results that corresponds to the LULC type-i from the field check results, x_{i+} is the LULC type-i from the simulation results, x_{+i} is the LULC type-i from the field check results, and *N* is all observation points.

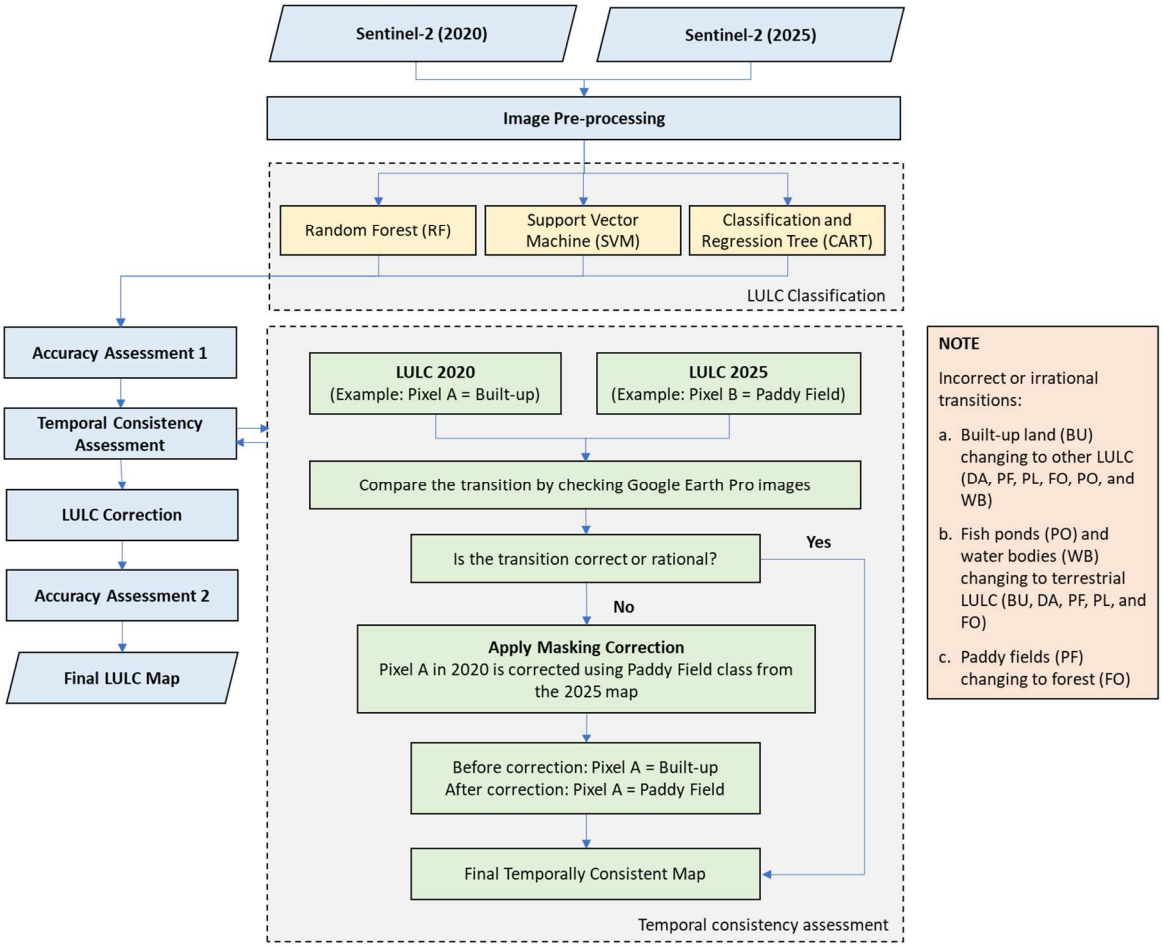

Figure 2. Research flowchart. This figure illustrates the workflow for LULC classification and temporal consistency assessment using Sentinel-2 imagery for 2020 and 2025. The process integrates machine learning algorithms (RF, SVM, and CART), followed by accuracy assessment, temporal consistency checking, and masking-based correction to address irrational transitions. The final output is a temporally consistent LULC map with improved classification reliability.

Temporal Consistency Assessment

The temporal consistency assessment was conducted to minimize inconsistent or irrational transitions between 2020 and 2025 and to improve the accuracy of the LULC classification. The 2020 LULC map was compared with the 2025 classification results to identify inconsistent or irrational LULC changes. During the study period (2020–2025), no major infrastructure or large-scale development projects were reported in the

study area that could have significantly altered land-use patterns within such a short time frameTherefore, several transitions were classified as irrational, including changes from BU to other LULC types (DA, PF, PL, FO, PO, and WB), given that built-up areas are generally considered nearly irreversible [39]. In addition, transitions from PO and WB to terrestrial LULC classes (BU, DA, PF, PL, and FO) were also regarded as unlikely due to the relatively stable nature of water-related land covers over time [40]. Furthermore, the conversion of PF into FO was considered implausible within a five-year period, as such natural succession processes typically require several decades [41].

Land Use/Land Cover Classification Correction

After identifying irrational transitions through the consistency assessment, masking was used to correct LULC consistency. For instance, in 2020, an area classified as BU was later classified as paddy fields in 2025. This transition was rechecked through visual interpretation of high-resolution imagery in Google Earth Pro for the corresponding location and time period. This verification indicated that the correct land cover was paddy fields. Therefore, the BU in the 2020 map was masked with the paddy field classification from the 2025 map because the transition from BU (2020) to PF (2025) was considered irrational. After correcting the classification results for all LULC classes, the final LULC map was obtained. The flowchart of this research is presented in Figure 2.

Results and Discussion

Results

The LULC classification results using RF, SVM, and CART for 2025, which consist of seven classes, are presented in Figure 3. Meanwhile, the area of LULC classification results for 2025 using RF, SVM, and CART is presented in Figure 4 and Table 2.

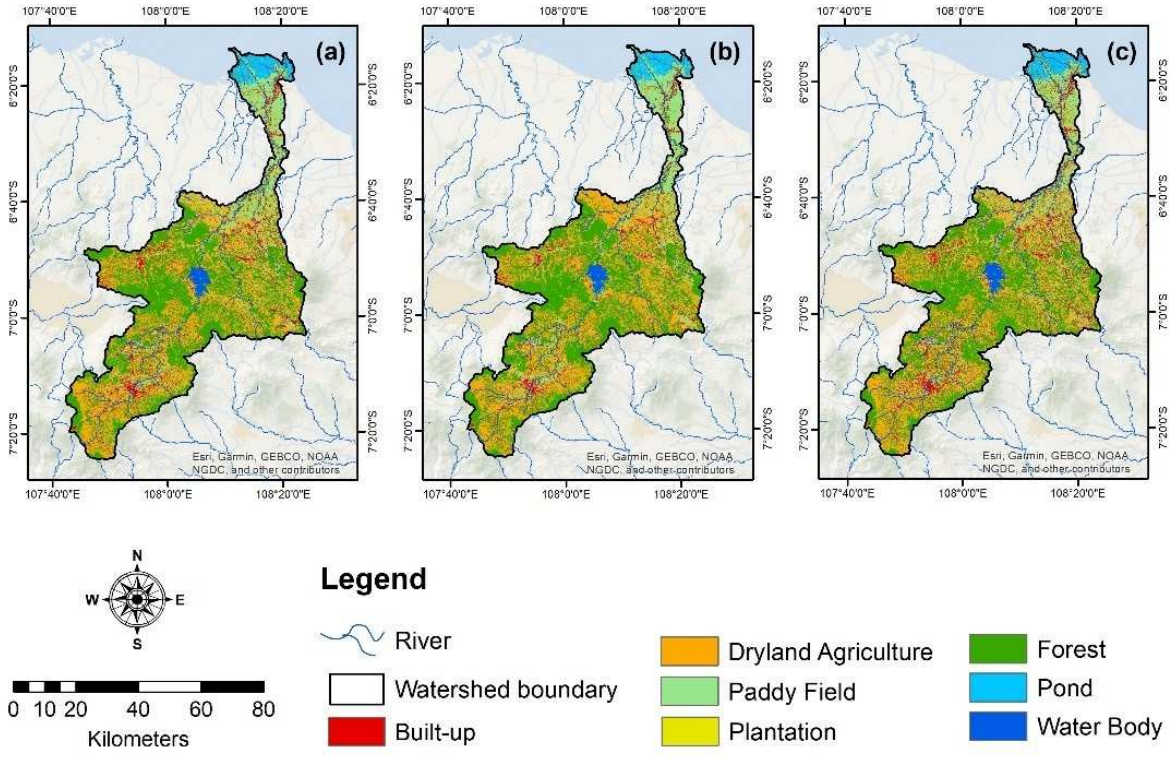

Figure 3. Map of LULC classification results for 2025 using (a) RF, (b) SVM, and (c) CART. Each map presents seven LULC classes, with paddy fields dominating the northern parts of the watershed. Forests mainly concentrated in the middle and southern areas. Meanwhile, built-up land scattered across urbanized zones. Ponds are primarily located in the northern region, reflecting coastal and lowland hydrological features.

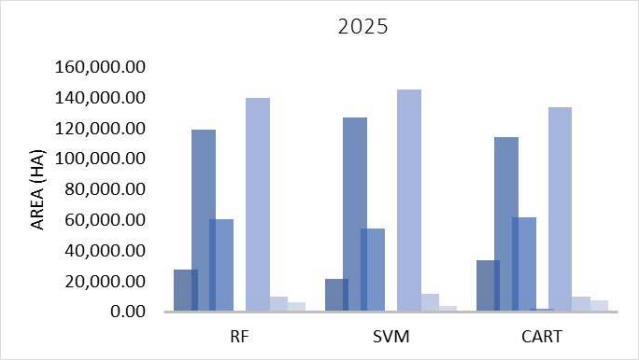

Figure 4. Area of LULC classification results for 2025 using RF, SVM, and CART. Across all classifiers, the LULC area shows the same order. The smallest are plantation, followed by water body, pond, built-up, paddy field, dryland agriculture, and the largest is forest.

Table 2. Area and percentage of LULC classification results for 2025 using RF, SVM, and CART. The Table showed that plantation has the smallest area percentage, at 0.16% (RF), 0% (SVM), and 0.6% (CART). Meanwhile, the forest has the highest area percentage at 38.42% (RF), 40.04% (SVM), and 36.83% (CART).

Class	RF		SVM		CART	
	Area (ha)	Percentage (%)	Area (ha)	Percentage (%)	Area (ha)	Percentage (%)
BU	27,408.45	7.54	21,291.77	5.86	33,631.01	9.25
DA	118,973.35	32.72	126,838.49	34.89	114,503.81	31.49
PF	60,703.16	16.70	54,673.05	15.04	61,973.56	17.05
PL	566.77	0.16	0.00	0.00	2,170.30	0.60
FO	139,672.63	38.42	145,555.23	40.04	133,907.08	36.83
PO	10,145.64	2.79	11,476.34	3.16	10,027.64	2.76
WB	6,098.47	1.68	3,733.58	1.03	7,355.08	2.02
Total	363,568.47	100.00	363,568.47	100.00	363,568.47	100.00

The lower part of the map (south) depicts the upstream area of the Cimanuk watershed, while the upper part (north) shows the downstream area. Forests and dryland agriculture dominate the upstream and middle sections of the watershed. The water body, the Jatigede Reservoir, is also situated in the central part of the Cimanuk watershed. Built-up areas are distributed throughout the watershed and are concentrated in the centres of Garut, Indramayu, Majalengka, and Sumedang regencies. Meanwhile, the downstream part of the watershed is mainly covered by paddy fields [42].

The RF classification results in 2020 are similar to those in 2025. According to Pande et al. [43], RF can produce stable LULC classification maps over multiple years. Meanwhile, SVM classification results in 2020 differ notably from those in 2025, with ponds and water bodies in 2020 being poorly classified. Similarly, CART in 2020 also failed to classify ponds and water bodies, as it did in 2025. The LULC classification maps for 2020, generated using RF, SVM, and CART classifiers, are shown in Figure 5.

Based on Table 3, RF achieved the highest accuracy in 2020, with 83.6% (OA) and 77.9% (KC), followed by CART with 68.9% (OA) and 58.6% (KC), and SVM with 68.9% (OA) and 56.9% (KC). Meanwhile, the highest accuracy in 2025 was achieved using RF classification, with an OA of 87.9% and a KC of 83.7%. The OA and KC for SVM ranked second at 85.0% and 79.8%, respectively. Meanwhile, the lowest OA and KC values were obtained with the CART classifier, at 82.8% and 77.1%, respectively. The superiority of RF over SVM and CART has also been reported in previous studies [44,45]. Research by Arpitha et al. [14] comparing the performance of RF, SVM, and CART over seven years using MSI's Sentinel-2 also consistently presented that RF could achieve the best results. On average, RF accuracy was about 5% higher for OA and 6.5% higher for Kappa than for the lowest-performing classifier (CART). The 2020 SVM and CART results have lower accuracy, likely due to greater spectral confusion among several LULC classes, cloud and shadow effects, as well as reduced class separability in the 2020 imagery. In contrast, the 2025 imagery provided clearer spectral distinction between classes, resulting in improved classification accuracy for all methods and OA values above 80%.

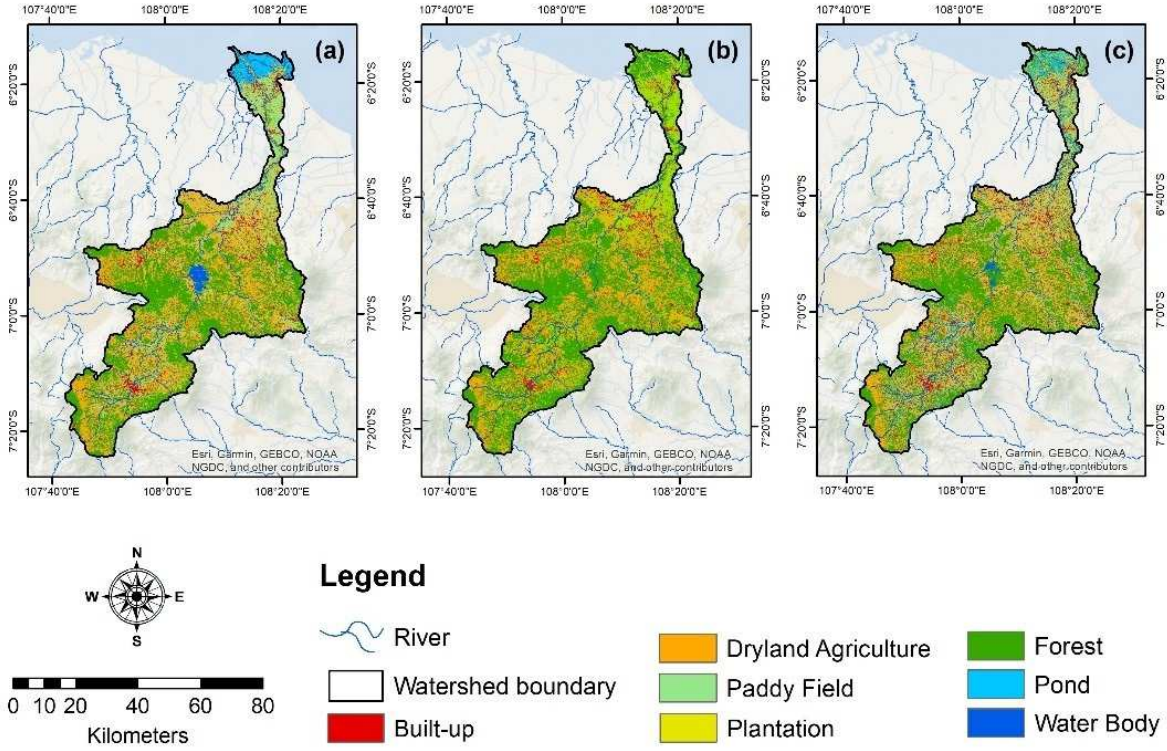

Figure 5. Map of LULC classification results for 2020 using (a) RF, (b) SVM, and (c) CART before consistency correction. The RF classification outputs for 2020 are comparable to those obtained for 2025. In contrast, SVM and CART exhibit clear inconsistencies, particularly in their inability to accurately identify ponds and water bodies in 2020, a limitation also observed in their 2025 results.

Table 3. Overall accuracy and Kappa coefficient of 2020 and 2025 LULC classification. In 2020, RF achieved the highest accuracy, outperforming CART and SVM. Similarly, in 2025, RF remained the most accurate, followed by SVM, while CART showed the lowest performance.

Year	Overall Accuracy (%)			Kappa Coefficient (%)		
	RF	SVM	CART	RF	SVM	CART
2020	83.6	68.9	68.9	77.9	56.9	58.6
2025	87.9	85.0	82.8	83.7	79.8	77.1

Based on the check for inconsistent or irrational transitions between 2020 and 2025 (Figure 6), CART results in more inconsistent or irrational transitions than RF and SVM, at 11.97%. SVM has the fewest inconsistent transitions, at 4.52%. This discrepancy is likely due to CART's reliance on a single decision tree, which is inherently more sensitive to noise and variations in the training data, often resulting in less stable classification. In contrast, RF combines multiple decision trees to reduce variance by aggregating multiple trees, while SVM demonstrates superior generalization capability through kernel-based class separation, resulting in more consistent classifications over time [37]. The area and percentage of inconsistent or irrational transitions from 2020 to 2025 are presented in Table 4.

A visual inspection of inconsistent transitions using multi-temporal high-resolution imagery from Google Earth Pro revealed that most irrational transitions were caused by misclassification rather than actual land-cover change. This is evident in Figure 7, where an examination of the 2025 high-resolution Google Earth imagery revealed classification errors and temporal inconsistencies at various locations in the 2020 map. Figure 7 also shows the improved classification results after applying the consistency correction masking to the LULC map.

A consistency correction was applied to the 2020 classification results by addressing irrational transitions. This correction successfully improved accuracy compared to the previous results. Overall and Kappa Coefficient for RF increased to 90% and 86.5%; SVM increased to 71.5% and 60.2%; and CART increased to 80.9% and 74.2%. The map after the consistency correction is shown in Figure 8. Although temporal consistency correction was applied, the 2020 image still had lower quality than the 2025 image, including stronger cloud-shadow effects, lower spectral contrast, and greater confusion between water-related and surrounding land-cover classes. As a result, the pond was more difficult to distinguish in the 2020 classification. RF was able to preserve the pond more clearly as its ensemble structure is more robust to image noise and spectral variability. In contrast, CART and SVM were more affected by lower image quality and confusion with adjacent classes, leading the pond to appear less distinct or to disappear after classification.

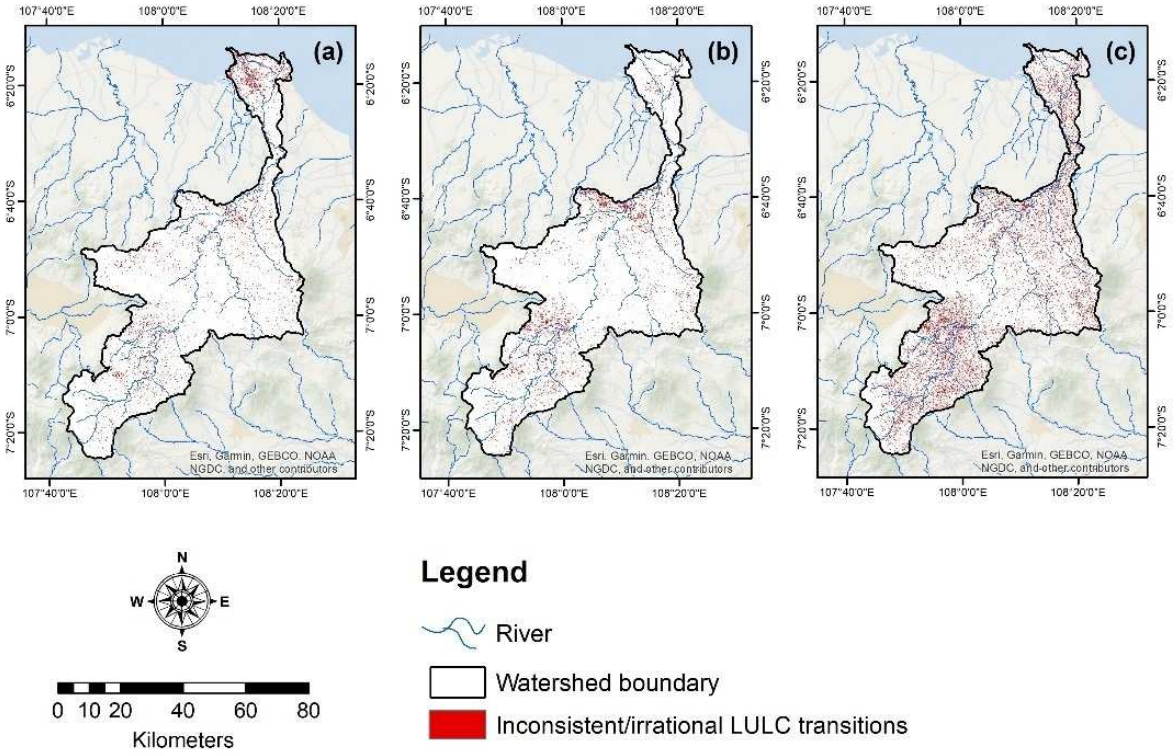

Figure 6. The inconsistent or irrational transition map from 2020 to 2025 using (a) RF, (b) SVM, and (c) CART. CART produced the highest proportion of inconsistent or irrational transitions, whereas SVM showed the lowest, with RF performing in between. This difference reflects CART's sensitivity to noise due to its single-tree structure, while RF and SVM provide more stable and consistent classifications through ensemble learning and kernel-based generalization.

Table 4. The area and percentage of rational and irrational transitions from 2020 to 2025. CART produced the highest proportion of irrational transitions, while SVM showed the lowest, with RF in between. This reflects CART's sensitivity to noise from its single-tree structure, whereas RF and SVM provide more stable results through ensemble learning and kernel-based generalization.

Class	RF		SVM		CART	
	Area (ha)	Percentage (%)	Area (ha)	Percentage (%)	Area (ha)	Percentage (%)
Rational transition	346,278.41	95.24	347,130.96	95.48	320,031.49	88.03
Irrational transition	17,290.06	4.76	16,437.51	4.52	43,536.98	11.97
Total	363,568.47	100.00	363,568.47	100.00	363,568.47	100.00

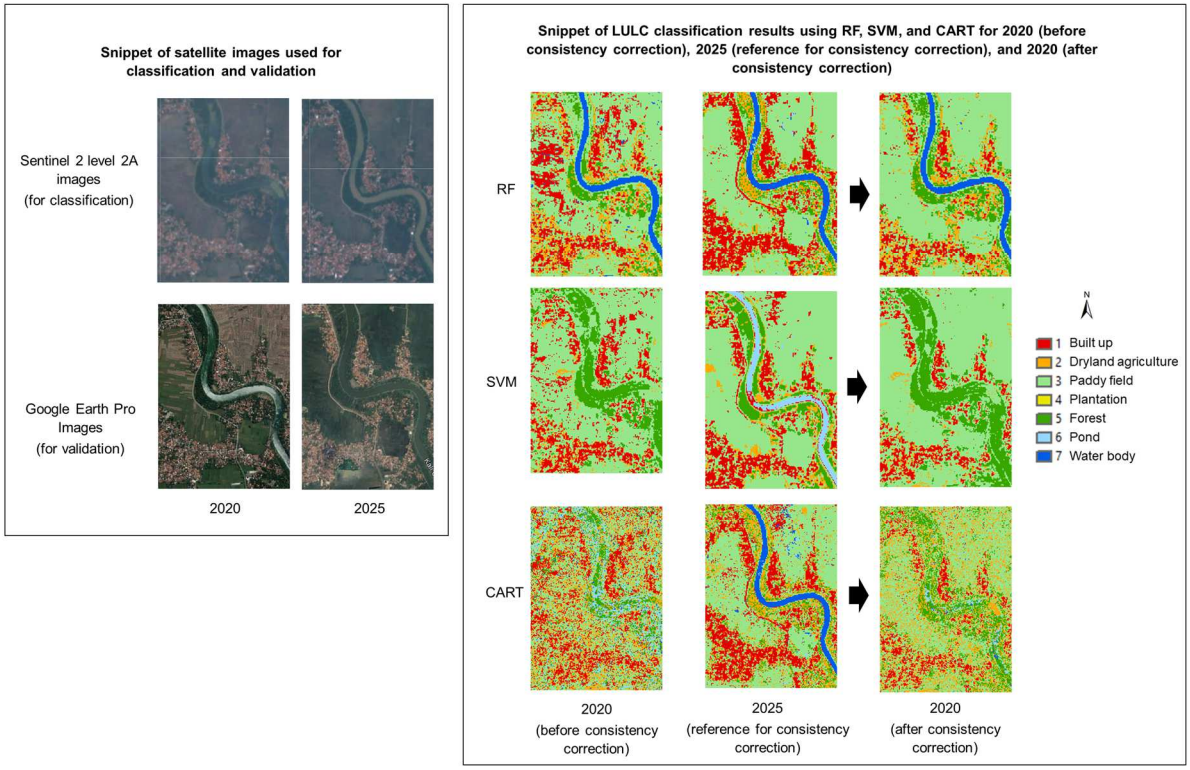

Figure 7. Snippet of satellite images and LULC classification results. Visual inspection using multi-temporal high-resolution imagery from Google Earth Pro indicates that most irrational transitions result from misclassification rather than actual land-cover change. Classification errors and temporal inconsistencies in the 2020 map are corrected after applying consistency masking, leading to improved LULC results.

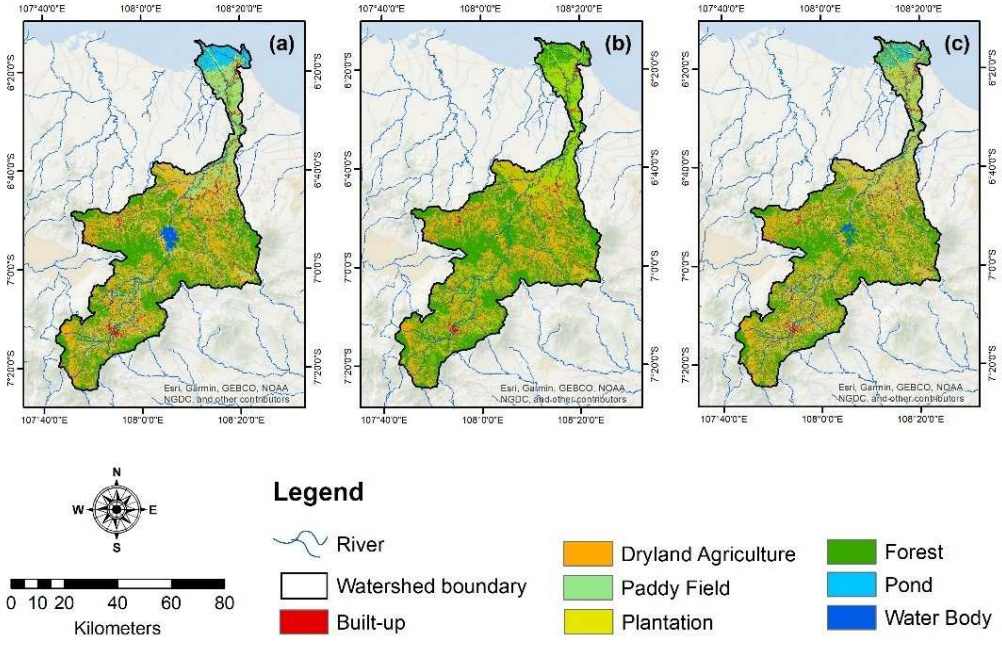

Figure 8. Map of the 2020 LULC classification results using (a) RF, (b) SVM, and (c) CART after consistency correction. The consistency correction successfully improved the accuracy compared to the previous results. However, lower 2020 image quality reduced class separability, especially for ponds, with RF remaining more robust, while SVM and CART were more affected by noise and spectral confusion.

Figure 9 shows the area of LULC before and after the temporal consistency correction. The total area produced by each method remains the same at 363,568.47 ha, although the area and percentage of each class varies across RF, SVM, and CART (Table 5 and 6). Typically, the RF, SVM, and CART classification methods produce the largest proportions of forest, dryland agriculture, paddy fields, and built-up areas. RF and SVM share the same order for classes five to seven, namely pond, water body, and plantation. Conversely, in CART, the order of classes five to seven is pond, plantation, and water body.

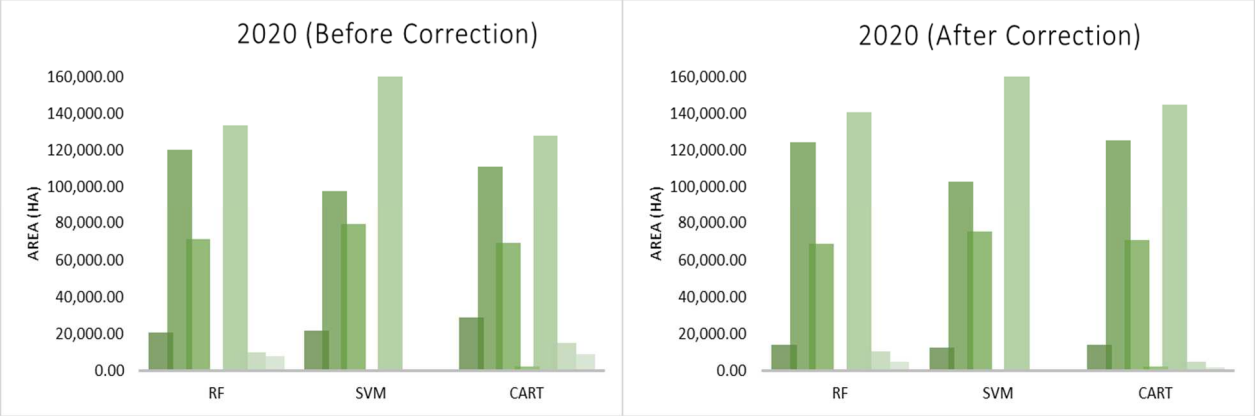

Figure 9. Map of the 2020 LULC classification results using RF, SVM, and CART before and after consistency correction. The map shows that consistency correction leads to noticeable adjustments in the area distribution of LULC classes across RF, SVM, and CART. After correction, class proportions become more consistent and balanced, indicating reduced misclassification. Overall, the correction improves the reliability of LULC area estimates for 2020.

Table 5. Area and percentage of LULC classification results for 2020 using RF, SVM, and CART before correction. The table shows that FO and DA are the most dominant land cover types across all three models, collectively accounting for over 60% of the total area. While RF and CART identify areas for all categories, SVM fails to detect any PL, PO, and WB. Overall, the models show the most consistency in classifying BU and PF, with only minor variations in their respective percentages.

Class	RF		SVM		CART	
	Area (ha)	Percentage (%)	Area (ha)	Percentage (%)	Area (ha)	Percentage (%)
BU	20,406.80	5.61	21,740.79	5.98	28,712.74	7.90
DA	120,603.03	33.17	97,746.23	26.89	111,279.93	30.61
PF	71,069.34	19.55	79,610.88	21.90	69,303.66	19.06
PL	325.26	0.09	0.00	0.00	2,279.36	0.63
FO	133,565.96	36.74	164,470.57	45.24	128,201.68	35.26
PO	9,947.28	2.74	0.00	0.00	15,054.33	4.14
WB	7,650.80	2.10	0.00	0.00	8,736.76	2.40
Total	363,568.47	100.00	363,568.47	100.00	363,568.47	100.00

Table 6. Area and percentage of LULC classification results for 2020 using RF, SVM, and CART after correction. After correction, FO and DA remain the most dominant land use categories, with all three models showing a slight increase in forest area compared to the previous results. While the SVM model now detects trace amounts of PO and WB, it still largely struggles to identify these smaller classes.

Class	RF		SVM		CART	
	Area (ha)	Percentage (%)	Area (ha)	Percentage (%)	Area (ha)	Percentage (%)
BU	13,946.77	3.84	12,669.16	3.48	13,757.42	3.78
DA	124,394.25	34.21	102,815.31	28.28	125,639.24	34.56
PF	68,958.15	18.97	75,538.70	20.78	70,851.96	19.49
PL	310.96	0.09	0.00	0.00	2,248.52	0.62

Class	RF		SVM		CART	
	Area (ha)	Percentage (%)	Area (ha)	Percentage (%)	Area (ha)	Percentage (%)
FO	140,817.68	38.73	172,494.77	47.44	144,850.35	39.84
PO	10,601.85	2.92	33.28	0.01	4,594.93	1.26
WB	4,538.81	1.25	17.25	0.00	1,626.06	0.45
Total	363,568.47	100.00	363,568.47	100.00	363,568.47	100.00

Discussion

The LULC classification results for 2025 in the Cimanuk watershed indicate that RF has the highest accuracy, followed by SVM and CART, with 87.9% (OA) and 83.7% (KC). RF also demonstrates the highest accuracy in the 2020 classification results, with 83.6% (OA) and 77.9% (KC). The superior performance of RF compared to the other two classifiers aligns with previous research findings [10,20,46]. RF has proven more stable at handling complex spatial data by building many decision trees and taking a majority vote.

Classification with SVM depends on the RBF kernel settings (gamma and cost values), so each classified image requires trial-and-error adjustments of gamma and cost to achieve the best classification results. In this study, the gamma and cost values from the reference (gamma = 1 and cost = 100) showed the best accuracy results from various experiments [18]. However, in 2025 and 2020, the SVM classification result did not include the plantation class. These results do not stem from insufficient training data, as the number of training and testing samples remained consistent across all classifiers. Instead, this discrepancy likely arises from spectral similarity between plantation areas and other vegetation classes, such as forests and dryland agriculture, which causes the SVM model to misclassify plantation pixels into these classes. Additionally, hyperparameter tuning was not performed in this study, as the SVM parameters (γ = 1 and C = 100) were adopted from previous studies reporting high classification accuracy. This indicates the need to tune gamma and cost values further to improve SVM classification in the Cimanuk watershed. Riaz et al. [47] stated that tuning the gamma and cost parameters in SVM becomes a crucial step involving testing and optimization, as it influences the model's performance.

The accuracy of CART and SVM decreased significantly in 2020 compared to 2025. Additionally, CART achieved slightly higher accuracy than SVM in 2020, whereas SVM outperformed CART in 2025. The differences in classification performance between CART and SVM from 2020 to 2025 were not caused by differences in the training dataset, as the same number and distribution of training samples were used for each LULC class in both years. Instead, the variation is likely related to differences in image quality. Although both classifications used Sentinel-2 Level-2A Surface Reflectance Harmonized imagery, the 2025 image exhibited clearer visual characteristics and better spectral separability among LULC classes than the 2020 image. In contrast, the 2020 image contained more noise and lower visual quality, which may have reduced classifiers' ability to separate classes accurately.

The temporal consistency analysis from 2020 to 2025 reveals that CART has the highest rate of irrational transitions (11.97%), followed by RF (4.76%) and SVM (4.52%). This suggests that, although CART's accuracy is moderate, it is most susceptible to producing irrational class transitions (e.g., from built-up areas to farmland). This is due to CART's high sensitivity to changes, which causes inconsistent classifications across two images [16]. Several dominant transitions identified in this study include: (1) BU changing to PF and DA, (2) PO or WB changing to PF and DA, and (3) PF changing directly to FO.

Temporal consistency correction was carried out by applying a mask to pixels identified as irrational transitions. This adjustment effectively improved the overall and Kappa Coefficient for RF, SVM, and CART. The accuracy gains highlight that temporal consistency correction is crucial for image classification to prevent irrational temporal transitions. Yang et al. [48] observed that several irrational transitions can occur in time-series classification outcomes, necessitating evaluation before deployment. In this study, after implementing temporal consistency correction, RF remained the top classifier with the highest accuracy, achieving 90% (OA) and 86.5% (KC), followed by CART (80.9% for OA and 74.2% for KC), and SVM (71.5% for OA and 60.2% for KC). The OA values were consistently higher than the Kappa coefficients for RF, SVM, and CART because OA measured the proportion of correctly classified samples, whereas the Kappa coefficient accounted for the agreement by chance. Consequently, Kappa provides a more conservative estimate of classification performance, particularly when class distributions are imbalanced, as is common in LULC datasets.

The improvement in OA and Kappa accuracy is particularly notable for the CART classifier because CART initially produced the highest proportion of inconsistent or irrational transitions among the three methods. The temporal consistency correction effectively reduced these unrealistic transitions by applying logical transition rules between 2020 and 2025, which corrected several misclassified pixels. As a result, the CART model indicates a larger increase in OA and Kappa than the other classifiers, indicating that the consistency correction is especially beneficial for classifiers that tend to produce more fragmented classification patterns.

Conclusions

This study compared the accuracy and temporal consistency between RF, SVM, and CART classifiers for LULC analysis in the Cimanuk watershed. The findings indicate that while RF achieved the highest classification accuracy, SVM demonstrated the highest level of temporal consistency, characterized by the fewest irrational transitions. In contrast, CART produced the highest proportion of irrational transitions. The findings further highlight the importance of incorporating temporal consistency analysis in LULC studies, which improved the accuracy of all classifiers and reduced misclassifications caused by ecologically unrealistic LULC transitions. These results provide more reliable LULC information that can support land-use planning, agricultural land protection, and disaster risk management in the Cimanuk watershed. The approach proposed in this study can also be implemented in other regions to improve the reliability of time-series LULC analysis. Future research is recommended to optimize classifier parameters, particularly gamma and cost, and to explore additional methods to enhance both classification accuracy and temporal consistency.

Author Contributions

SDA: Conceptualization, Methodology, Software, Data Analysis, Writing; **WDA:** Conceptualization, Methodology, Writing - Review & Editing; **WAM:** Conceptualization, Methodology, Writing - Review & Editing; **IN**: Writing - Review & Editing; **DLC**: Writing - Review & Editing; **AF**: Writing - Review & Editing; and **YS**: Writing - Review & Editing.

AI Writing Statement

During the preparation of this work, the authors used Grammarly for language editing and proofreading. After using this tool/service, the authors reviewed and edited the content as needed and take full responsibility for the content of the publication.

Conflicts of interest

There are no conflicts to declare.

Acknowledgments

Thank you to the Research and Innovation Agency (BRIN) for their support with facilities and resources in the Postdoctoral 2025 program. Thanks, are also extended to the GEE platform developer, the European Space Agency, the Geospatial Information Agency, the Central Statistics Agency, and Google Earth Pro for providing the data. Additionally, gratitude is expressed to all parties involved in the writing of this scientific journal article.

References

1. Krisnanta, A.D.; Hasibuan, H.S.; Tambunan, R.P. Analysis of Landcover Changes and Carrying Capacity of Coastal Cities North Java of Central Java Province, Indonesia. *J. Pengelolaan Sumberd. Alam dan Lingkung.* **2024**, *14*, 181–189, doi:10.29244/jpsl.14.1.181.
2. Bondansari; Widiatmaka; Machfud; Munibah, K.; Ambarwulan, W. Preserving Rice Fields and Domestic Rice Adequacy: A Case Study in Banyumas Regency, Central Java, Indonesia. *J. Pengelolaan Sumberd. Alam dan Lingkung.* **2025**, *15*, 154–165, doi:10.29244/jpsl.15.1.154.

3. Supangat, A.B.; Basuki, T.M.; Indrajaya, Y.; Setiawan, O.; Wahyuningrum, N.; Purwanto; Putra, P.B.; Savitri, E.; Indrawati, D.R.; Auliyani, D.; et al. Sustainable Management for Healthy and Productive Watersheds in Indonesia. *Land* **2023**, *12*, 1–34, doi:10.3390/land12111963.
4. Ambarwulan, W.; Yulianto, F.; Widiatmaka, W.; Rahadiati, A.; Tarigan, S.D.; Firmansyah, I.; Hasibuan, M.A.S. Modelling Land Use/Land Cover Projection Using Different Scenarios in the Cisadane Watershed, Indonesia: Implication on Deforestation and Food Security. *Egypt. J. Remote Sens. Sp. Sci.* **2023**, *26*, 273–283, doi:10.1016/j.ejrs.2023.04.002.
5. Nahib, I.; Ambarwulan, W.; Rahadiati, A.; Munajati, S.L.; Prihanto, Y.; Suryanta, J.; Turmudi, T.; Nuswantoro, A.C. Assessment of the Impacts of Climate and LULC Changes on the Water Yield in the Citarum River Basin, West Java Province, Indonesia. *Sustain.* **2021**, *13*, 1–20, doi:10.3390/su13073919.
6. Setyorini, A.; Khare, D.; Pingale, S.M. Simulating the Impact of Land Use/Land Cover Change and Climate Variability on Watershed Hydrology in the Upper Brantas Basin, Indonesia. *Appl. Geomatics* **2017**, *9*, 191–204, doi:10.1007/s12518-017-0193-z.
7. Fakhrudin, M.; Daruati, D. Zonasi Resapan Air Hujan Sebagai Dasar Konservasi Sumber Daya Air DAS Cimanuk. *LIMNOTEK Perair. Darat Trop. Indones.* **2017**, *24*, 26–35.
8. Ridwansyah, I.; Yulianti, M.; Apip; Onodera, S. ichi; Shimizu, Y.; Wibowo, H.; Fakhrudin, M. The Impact of Land Use and Climate Change on Surface Runoff and Groundwater in Cimanuk Watershed, Indonesia. *Limnology* **2020**, *21*, 487–498, doi:10.1007/s10201-020-00629-9.
9. Mashala, M.J.; Dube, T.; Ayisi, K.K.; Ramudzuli, M.R. Using the Google Earth Engine Cloud-Computing Platform to Assess the Long-Term Spatial Temporal Dynamics of Land Use and Land Cover within the Letaba Watershed, South Africa. *Geocarto Int.* **2023**, *38*, 1–20, doi:10.1080/10106049.2023.2252781.
10. Loukika, K.N.; Keesara, V.R.; Sridhar, V. Analysis of Land Use and Land Cover Using Machine Learning Algorithms on Google Earth Engine for Munneru River Basin, India. *Sustain.* **2021**, *13*, 1–15.
11. Gautam, L.; Rai, R. Land Use and Land Cover Change Analysis Using Google Earth Engine in Manamati Watershed of Kathmandu District, Nepal. *Third Pole J. Geogr. Educ.* **2022**, *22*, 49–60, doi:10.3126/ttp.v22i01.52560.
12. Gorelick, N.; Hancher, M.; Dixon, M.; Ilyushchenko, S.; Thau, D.; Moore, R. Google Earth Engine: Planetary-Scale Geospatial Analysis for Everyone. *Remote Sens. Environ.* **2017**, *202*, 18–27, doi:10.1016/j.rse.2017.06.031.
13. Tamiminia, H.; Salehi, B.; Mahdianpari, M.; Quackenbush, L.; Adeli, S.; Brisco, B. Google Earth Engine for Geo-Big Data Applications: A Meta-Analysis and Systematic Review. *ISPRS J. Photogramm. Remote Sens.* **2020**, *164*, 152–170, doi:10.1016/j.isprsjprs.2020.04.001.
14. Arpitha, M.; Ahmed, S.A.; Harishnaika, N. Land Use and Land Cover Classification Using Machine Learning Algorithms in Google Earth Engine. *Earth Sci. Informatics* **2023**, *16*, 3057–3073, doi:10.1007/s12145-023-01073-w.
15. Maxwell, A.E.; Warner, T.A.; Fang, F. Implementation of Machine-Learning Classification in Remote Sensing: An Applied Review. *Int. J. Remote Sens.* **2018**, *39*, 2784–2817, doi:10.1080/01431161.2018.1433343.
16. Gülci, S.; Wing, M.; Akay, A.E. Land Use and Land Cover (LULC) Mapping Accuracy Using Single-Date Sentinel-2 MSI Imagery with Random Forest and Classification and Regression Tree Classifiers. *Geomatics* **2025**, *5*, 1–20, doi:10.3390/geomatics5030029.
17. Sundar, P.K.S.; Deka, P.C. Spatio-Temporal Classification and Prediction of Land Use and Land Cover Change for the Vembanad Lake System, Kerala: A Machine Learning Approach. *Environ. Sci. Pollut. Res.* **2022**, *29*, 86220–86236, doi:10.1007/s11356-021-17257-0.
18. Prodromou, M.; Gitas, I.; Mettas, C.; Tzouvaras, M.; Danezis, C.; Hadjimitsis, D. Comparative Analysis of Supervised Machine Learning Algorithms for Forest Habitat Mapping in Cyprus. *Sustain.* **2025**, *17*, 1–32, doi:10.3390/su17136021.
19. Xie, G.; Niculescu, S. Mapping and Monitoring of Land Cover/Land Use (LCLU) Changes in the Crozon Peninsula (Brittany, France) from 2007 to 2018 by Machine Learning Algorithms (Support Vector Machine, Random Forest, and Convolutional Neural Network) and by Post-Classification C. *Remote Sens.* **2021**, *13*, 1–23, doi:10.3390/rs13193899.

20. Zafar, Z.; Zubair, M.; Zha, Y.; Fahd, S.; Ahmad Nadeem, A. Performance Assessment of Machine Learning Algorithms for Mapping of Land Use/Land Cover Using Remote Sensing Data. *Egypt. J. Remote Sens. Sp. Sci.* **2024**, *27*, 216–226, doi:10.1016/j.ejrs.2024.03.003.
21. Pan, X.; Wang, Z.; Feng, G.; Wang, S.; Samiappan, S. Automated Mapping of Land Cover in Google Earth Engine Platform Using Multispectral Sentinel-2 and MODIS Image Products. *PLoS One* **2025**, *20*, 1–21, doi:10.1371/journal.pone.0312585.
22. Zhong, B.; Yang, A.; Jue, K.; Wu, J. Long Time Series High-Quality and High-Consistency Land Cover Mapping Based on Machine Learning Method at Heihe River Basin. *Remote Sens.* **2021**, *13*, 1–18, doi:10.3390/rs13081596.
23. Zhu, L.; Liu, J.; Jiang, S.; Zhang, J. Improvement of Spatio-Temporal Inconsistency of Time Series Land Cover Products. *Sustain.* **2024**, *16*, 1–23, doi:10.3390/su16188127.
24. Heryani, N.; Kartiwa, B.; Sosiawan, H.; Rejekiningrum, P.; Adi, S.H.; Apriyana, Y.; Pramudia, A.; Yufdy, M.P.; Tafakresnanto, C.; Rivaie, A.A.; et al. Analysis of Climate Change Impacts on Agricultural Water Availability in Cimanuk Watershed, Indonesia. *Sustain.* **2022**, *14*, 1–18, doi:10.3390/su142316236.
25. ESA (European Space Agency). Sentinel-2 MSI Level-2A Surface Reflectance Harmonized. Available online: https://developers.google.com/earth-engine/datasets/catalog/COPERNICUS_S2_SR_HARMONIZED (accessed on 10 October 2025).
26. Google. Google Earth Pro (High-Resolution Satellite Imagery). Available online: https://www.google.com/earth/about/versions/#earth-pro (accessed on 20 October 2025).
27. BIG (Badan Informasi Spasial). Rupa Bumi Indonesia (RBI) Map, Scale 1:25,000. Available online: https://tanahair.indonesia.go.id/portal-web/ (accessed on 8 April 2026).
28. Joyce, A.T. *Procedures for Gathering Ground Truth Information for a Supervised Approach to a Computer-Implemented Land Cover Classification of Landsat-Acquired Multispectral Scanner Data*; NASA: Washington DC, USA, 1978; ISBN 9780874216561.
29. Dash, P.; Sanders, S.L.; Parajuli, P.; Ouyang, Y. Improving the Accuracy of Land Use and Land Cover Classification of Landsat Data in an Agricultural Watershed. *Remote Sens.* **2023**, *15*, 1–24, doi:10.3390/rs15164020.
30. Zhao, J.; Wang, L.; Yang, H.; Wu, P.; Wang, B.; Pan, C.; Wu, Y. A Land Cover Classification Method for High-Resolution Remote Sensing Images Based on NDVI Deep Learning Fusion Network. *Remote Sens.* **2022**, *14*, 1–19, doi:10.3390/rs14215455.
31. Breiman, L.; Friedman, J.H.; Olshen, R.A.; Stone, C.J. *Classification and Regression Trees*; Chapman & Hall/CRC: Boca Raton, USA, 1984; ISBN 9780412048418.
32. Cortes, C.; Vapnik, V. Support-Vector Networks. *Mach. Learn.* **1995**, *20*, 273–297, doi:10.1109/64.163674.
33. Kasahun, M.; Legesse, A. Machine Learning for Urban Land Use/ Cover Mapping: Comparison of Artificial Neural Network, Random Forest and Support Vector Machine, a Case Study of Dilla Town. *Heliyon* **2024**, *10*, e39146, doi:10.1016/j.heliyon.2024.e39146.
34. Chung, L.C.H.; Xie, J.; Ren, C. Improved Machine-Learning Mapping of Local Climate Zones in Metropolitan Areas Using Composite Earth Observation Data in Google Earth Engine. *Build. Environ.* **2021**, *199*, 107879, doi:10.1016/j.buildenv.2021.107879.
35. Savas, C.; Dovis, F. The Impact of Different Kernel Functions on the Performance of Scintillation Detection Based on Support Vector Machines. *Sensors (Switzerland)* **2019**, *19*, 1–16, doi:10.3390/s19235219.
36. Abedinia, A.; Seydi, V. Building Semi-Supervised Decision Trees with Semi-Cart Algorithm. *Int. J. Mach. Learn. Cybern.* **2024**, *15*, 4493–4510, doi:10.1007/s13042-024-02161-z.
37. Belgiu, M.; Drăgut, L. Random Forest in Remote Sensing: A Review of Applications and Future Directions. *ISPRS J. Photogramm. Remote Sens.* **2016**, *114*, 24–31, doi:10.1016/j.isprsjprs.2016.01.011.
38. Tilahun, A.; Teferie, B. Accuracy Assessment of Land Use Land Cover Classification Using Google Earth. *Am. J. Environ. Prot.* **2015**, *4*, 193–198, doi:10.11648/j.ajep.20150404.14.

39. Gao, J.; O'Neill, B.C. Mapping Global Urban Land for the 21st Century with Data-Driven Simulations and Shared Socioeconomic Pathways. *Nat. Commun.* **2020**, *11*, 1–12, doi:10.1038/s41467-020-15788-7.

40. Bojago, E.; Tadila, G.; Masha, M. Monitoring Spatio-Temporal Changes in Land Use, Land Cover, and NDVI Using MODIS Data in Ethiopia's Gambela Region. *Discov. Appl. Sci.* **2025**, *7*, 1–19, doi:10.1007/s42452-025-07879-1.

41. Cao, G.; Tsuchiya, K.; Zhu, W.; Okuro, T. Vegetation Dynamics of Abandoned Paddy Fields and Surrounding Wetlands in the Lower Tumen River Basin, Northeast China. *PeerJ* **2019**, *2019*, 1–17, doi:10.7717/peerj.6704.

42. Ardiansyah, M.; Nugraha, R.A.; Iman, L.O.S.; Djatmiko, S.D. Impact of Land Use and Climate Changes on Flood Inundation Areas in the Lower Cimanuk Watershed, West Java Province. *J. Ilmu Tanah dan Lingkung.* **2021**, *23*, 51–58, doi:10.29244/jitl.23.2.53-60.

43. Pande, C.B.; Srivastava, A.; Moharir, K.N.; Radwan, N.; Sidek, L.M.; Alshehri, F.; Pal, S.C.; Tolche, A.D.; Zhran, M. Characterizing Land Use/Land Cover Change Dynamics by an Enhanced Random Forest Machine Learning Model: A Google Earth Engine Implementation. *Environ. Sci. Eur.* **2024**, *36*, 1–23, doi:10.1186/s12302-024-00901-0.

44. Amin, G.; Imtiaz, I.; Haroon, E.; Saqib, N. us; Shahzad, M.I.; Nazeer, M. Assessment of Machine Learning Algorithms for Land Cover Classification in a Complex Mountainous Landscape. *J. Geovisualization Spat. Anal.* **2024**, *8*, 1–19, doi:10.1007/s41651-024-00195-z.

45. Farikhi, F.A.; Pramono, R.W.D. Perbandingan Algoritma Classification and Regression Tree (Cart) Dan Random Forest (Rf) Untuk Klasifikasi Penggunaan Lahan Pada Google Earth Engine. *J. Spat. Wahana Komun. dan Inf. Geogr.* **2023**, *23*, 170–179, doi:10.21009/spatial.232.09.

46. Khan, S.; Bhardwaj, A.; Sakthivel, M. Accuracy Assessment of Land Use Land Cover Classification Using Machine Learning Classifiers in Google Earth Engine; A Case Study of Jammu District. In Proceeding of ISPRS TC IV Mid-term Symposium "Spatial Information to Empower the Metaverse", Perth, Australia, 22–25 October 2024; pp. 263–268.

47. Riaz, M.T.; Riaz, M.T.; Rehman, A.; Bindajam, A.A.; Mallick, J.; Abdo, H.G. An Integrated Approach of Support Vector Machine (SVM) and Weight of Evidence (WOE) Techniques to Map Groundwater Potential and Assess Water Quality. *Sci. Rep.* **2024**, *14*, 26186, doi:10.1038/s41598-024-76607-3.

48. Yang, G.; Fang, S.; Gong, W.; Zhao, Y.; Ge, M. Evaluating the Reliability of Time Series Land Cover Maps by Exploiting the Hidden Markov Model. *Stoch. Environ. Res. Risk Assess.* **2020**, *35*, 881–892, doi:10.1007/s00477-020-01915-9.